Smart Structures and Systems, *Vol. 36, No. 5 (2025) 253-263*
https://doi.org/10.12989/sss.2025.36.5.253

Markerless LED-based geometric calibration for high-precision image acquisition in structural inspection

Jinho Song [1a], Sangmok Lee [2b], Jaewon Park [1c], In-Ho Kim[**3] and Sungsik Yoon[*1]

[1] *Department of Artificial Intelligence, Hannam University, 70 Hannam-ro, Daejeon 34430, Republic of Korea*
[2] *Dam Safety Management Center, Korea Water Resources Corporation (K-water), 200 Sintanjin-ro, Daejeon 34350, Republic of Korea*
[3] *Department of Civil Engineering, Kunsan National University, 558 Daehak-ro, Kunsan 54150, Republic of Korea*

(*Received August 18, 2025, Revised November 20, 2025, Accepted November 26, 2025*)

Abstract. This study proposes an image acquisition system that aims to correct geometric distortion of images for the structure inspection. The proposed system is composed of main camera, light-emitting diode module, the displacement sensor, and the movement system. Most images taken in the industrial environment are typically distorted, which increase difficulty of damage inspection. Thus, calibration procedure is required to correct distortion. However, two main problems remain: (1) most existing studies focus on lens distortion without considering geometric distortions caused by camera angles, and (2) most image acquisition systems rely on markers such as checkerboard, which increase inconvenience. Therefore, the proposed image acquisition system is developed to ease these problems. The proposed system employs an LED module to project a specialized light pattern instead of using physical markers, and geometric calibration can be performed by selecting corner points of the projected pattern. Furthermore, the movement system supports linear movement up to 3000 mm and full 360° rotation, producing flexibility in experimental setups. Thus, experts are able to perform precise inspection with simple image pre-processing. Experiments are conducted in both indoor and outdoor environments, and results prove the effectiveness of the proposed image acquisition system by achieving better root mean square error.

Keywords: geometric calibration; image acquisition system; markerless LED; perspective transformation; structural inspections

1. Introduction

Concrete is one of the most widely used construction materials in engineering, offering high strength and durability. It is commonly employed in various infrastructure systems such as bridges, buildings, and roads. However, as these concrete-based infrastructures age, increasing attention has been directed toward their inspection and maintenance, leading to a growing body of related research (Yoon *et al*. 2021a, b). In particular, large-scale structures such as steel bridges are susceptible to damage due to continuous loading and environmental factors. Therefore, early detection and timely repair of such damage are essential to ensure structural safety. (Yoon *et al*. 2022a, b)

Structural damage inspections involve identifying potential damage through on-site surveys, followed by appropriate maintenance actions. Surface damage on infrastructures typically results from inadequate management or environmental factors. Especially, factors such as temperature fluctuations, moisture, mechanical loads, and external impacts can lead to the formation of cracks (Munawar *et al*. 2022). These cracks not only compromise the structural integrity of the system but also increase maintenance costs, and if left unaddressed, may ultimately lead to catastrophic failures (Kaveh and Alhajj 2024, Yoon *et al*. 2018). Therefore, early detection and proper management of cracks in infrastructure—such as concrete structures and steel bridges—are essential for ensuring safety and long-term durability (Yoon *et al*. 2020a, b).

Various types of data are used to detect crack or damage such as vibration data (Ali *et al*. 2019, Rehman *et al*. 2024), and the most common inspection method for crack identification is visual inspection, in which experts directly examine the structure to assess the presence and condition of cracks (Yuan *et al*. 2024). However, this method suffers from low reliability, as the results depend on the expert's experience and condition. Moreover, due to the structural characteristics of many infrastructures, they are often designed in ways that limit physical access, making inspection difficult (Moore *et al*. 2001). In addition, large-scale structure inspection requires considerable time and cost, leading to concerns regarding the economic feasibility of such methods (Xu and Turkan 2020). Therefore, the development of efficient and reliable crack detection technologies is necessary.

*Corresponding author, Assistant Professor,
E-mail: sungsik@hnu.kr
**Co-corresponding author, Associate Professor,
E-mail: inho.kim@kunsan.ac.kr
[a] Assistant Professor, E-mail: samuel9157@hnu.kr
[b] Senior Researcher
[c] Undergraduate Student

ISSN: 1738-1584 (Print), 1738-1991 (Online)

2. Related works

Research on image-based inspection algorithms and hardware systems has been actively conducted for several decades. Thus, the literature in this field has become increasingly diverse and vast. In this paper, related studies on crack identification are broadly classified into two categories: algorithmic approaches and hardware-based systems. The former focuses on developing computational methods for identifying and quantifying cracks from visual data such as RGB images, while the latter emphasizes the design and implementation of specialized devices or sensing systems that facilitate data acquisition.

In algorithmic approaches, classic computer vision algorithms are developed and applied to effectively detect crack on various structures. Kim *et al*. (2017b) and Zhu *et al*. (2018) proposed the binarization methods that automatically determines threshold values which results can vary and fail since the algorithms depend on the parameter. Tian *et al*. (2019) not only use binarization but also propose stitching method using the scale-invariant feature transform (SIFT) algorithm. Similarly, Li *et al*. (2023) applies image registration method to detect and measure crack widths using SIFT method for close-up and long-range images. Lee *et al*. (2021) proposed de-blur algorithms for bridge damage inspection method by estimating blur kernel. Note that the classic computer vision algorithms such as Otsu and SIFT methods are still actively used in crack identification due to its computation efficiency and reasonably balanced accuracy.

Since AlexNet is introduced (Krizhevsky *et al*. 2012), deep neural networks have been actively applied in various industrial environments, including crack identification. Dorafshan *et al*. (2018) compares edge detection methods to convolutional neural networks (CNNs) and conclude that CNN in transfer learning module performed better than other edge detection methods. Then, variety of CNN-based architecutres such as U-Net, Mask R-CNN, and YOLO have been adopted for crack identification and segmentation (e.g. Bhowmick *et al*. 2020, Zhang *et al*. 2021, Kumar *et al*. 2021, Ni *et al*. 2023, Wang *et al*. 2023, Feng *et al*. 2024, Peng *et al*. 2024, Kang and An 2024). Also, since transformer proved its efficient performance (Dosovitskiy *et al*. 2020) in computer vision, transformer architectures are recently applied and used to crack identification in various papers (Ding *et al*. 2023, Meng *et al*. 2024, Tanveer and Cho 2025).

In order to capture and collect images from various structures, various types of hardware systems have been developed for image acquisition. The most common platform is Unmanned aerial vehicle (UAV), which enables access to areas that human is difficult to reach. Some studies utilize UAV system equipped only with camera module to collect images (Bhowmick *et al*. 2020, Lee *et al*. 2021, Feng *et al*. 2024). However, in many cases, laser range finder or displacement sensor is attached to measure crack widths (Zhong *et al*. 2018, Ding *et al*. 2023, Kim *et al*. 2017a, Tian *et al*. 2019). In some settings, various additional components such as GPS module, Wi-Fi module or Barometer are attached (Lei et al. 2020). Moreover, not all image acquisition systems use UAVs. For example, Tian *et al*. (2019) proposed a ground-based system that is composed of main camera and laser ranging finder.

Systems using camera modules typically require a calibration process to correct lens distortion. This calibration generally depends on physical markers such as checkerboard patterns or red dot targets (Kim *et al*. 2017a, Ding *et al*. 2023, Feng *et al*. 2024). But, using physical markers constraints accessibility and convenience since there are places that human is difficult to reach to place markers in industrial environments such as ceiling or bridge structures. In addition, the previous researches do not consider other geometric correction, which can lead to inaccuracies in measurement results as shown in Fig. 1. In particular, distortion often arises from oblique camera angles, which can degrade the performance of identification algorithms. The most effective way to minimize such distortion is to capture images with the camera directly oriented perpendicular to the target; however, this is often impractical in real-world inspections such as bolt or crack width estimation.

Moreover, UAV systems have advantages in accessing various areas, but face limitations in maintaining stable distance and orientation near the inspection surface. Also factors such as wind, vibration, and operator control can cause unintended geometric distortion. These limitations require a stable ground-based inspection system.

To ease the problem, this paper proposes an inspection methodology using a marker-free image acquisition system that eliminates the need for physical markers. The proposed system is designed to minimize distortion and enable accurate crack measurement through a structured-light projection using an LED module, thereby proposing a calibration method that does not require physical targets improving usability and practicality in real-world inspection scenarios. The main contributions are as follows:

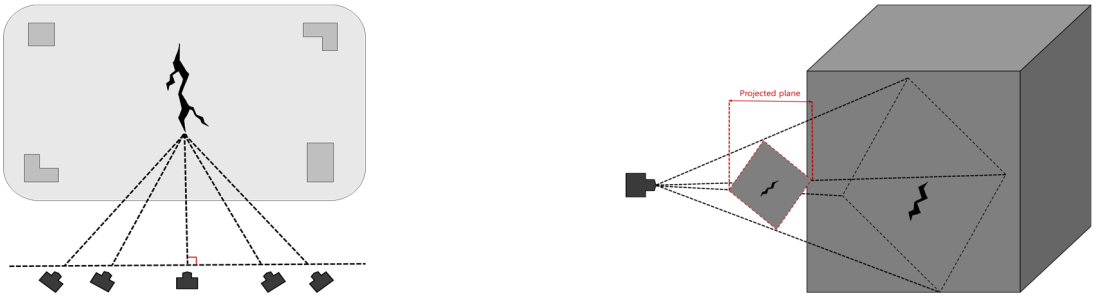

Fig. 1 Illustrations of geometric distortion due to camera angle

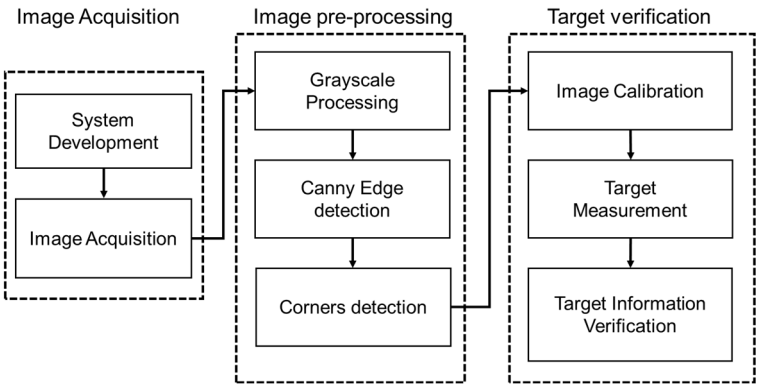

Fig. 2 The flowchart of the proposed methodology

- The image acquisition system is proposed that does not require physical markers for calibration, which increase accessibility and convenience for inspection.
- The flexible inspection framework is proposed which the algorithmic components can be replaced or upgraded as needed.

3. Proposed methodology

The proposed methodology consists of three main steps: image acquisition, image pre-processing, and target verification as illustrated in Fig. 2. In the image acquisition step, raw images are obtained using the proposed marker-free acquisition system. Next, image pre-processing is applied to detect the corners of the projected pattern. Finally, target verification is conducted to apply calibration and measure the inspected features, such as cracks or bolts. In the following subsections, the image acquisition system is first introduced, followed by a description of the overall framework for the methodology.

3.1 Design and components of the image acquisition system

The proposed image acquisition system, which represents the main contribution of this study, is composed of four core components: a high-resolution camera (Canon M10), a light-emitting diode (LED) module (Thorlabs MWWHLP1), a displacement sensor (Sony ILCE-7C), and a movement system, as illustrated in Fig. 3(a).

The camera serves as the primary imaging device, capable of capturing detailed surface textures and fine structural features for subsequent crack detection and measurement. The LED module, mounted on the Resolv4k lens system, projects a structured light pattern onto the target surface, enhancing feature visibility and enabling precise geometric analysis. Its illuminance can be adjusted through an LED driver (Fig. 3(b)), ensuring optimal lighting under varying ambient illumination levels. The displacement sensor measures the distance between the imaging device and the target surface, ensuring precise distance control between the camera and the inspection area. The specifications of main camera and LED module are summarized in Table 1.

The movement system, a key component of the proposed image acquisition system, is designed to provide flexible positioning of the acquisition components, enabling accurate inspection across various target types and environments. As shown in Fig. 4(a), the movement system consists of three main components: the sensor module support, the linear movement guide rail, and the target support. The sensor module comprises the camera, LED projection module, and displacement sensor, all mounted on a rigid support frame. This support is installed on a wheel-mounted linear movement guide rail, equipped with a 1,500 mm ruler for precise position control, allowing translation from 1,500 mm to 3,000 mm and enabling full 360° rotational movement around the main target.

The guide rail is connected to the target support, which has dimensions of 1,000 mm × 1,000 mm × 16.5 mm. The target support can securely hold various inspection surfaces, accommodating a wide range of structures. As illustrated in Fig. 4(b), a steel plate is mounted as the inspection target to the support system, but the system can also be adapted for concrete panels, tunnel segments, or other structures. This wheel-mounted and modular configuration facilitates image acquisition from multiple angles and positions, ensuring adaptability for both controlled indoor experiments and large-scale outdoor inspections.

3.2 Image acquisition and image pre-processing

Images are first captured using the proposed image acquisition system, including a reference image taken with the camera oriented perpendicular to the target. Subsequently, an image pre-processing procedure is applied to detect and measure the four corners of the projected pattern. The pre-processing pipeline proceeds as follows. First, the captured image is converted to grayscale, and the Canny edge detection algorithm (Canny 1986) is applied. The Canny algorithm consists of four main steps: (1) a Gaussian filter to decrease noise, (2) the gradient magnitude and direction computation for each pixel, (3) edge candidates selection based on gradient information, and (4) the final edge map computation based on user defined thresholds. Once the edges are detected, the user manually selects the four corners of the pattern, as illustrated in Fig. 5. Although the current implementation relies on manual selection for

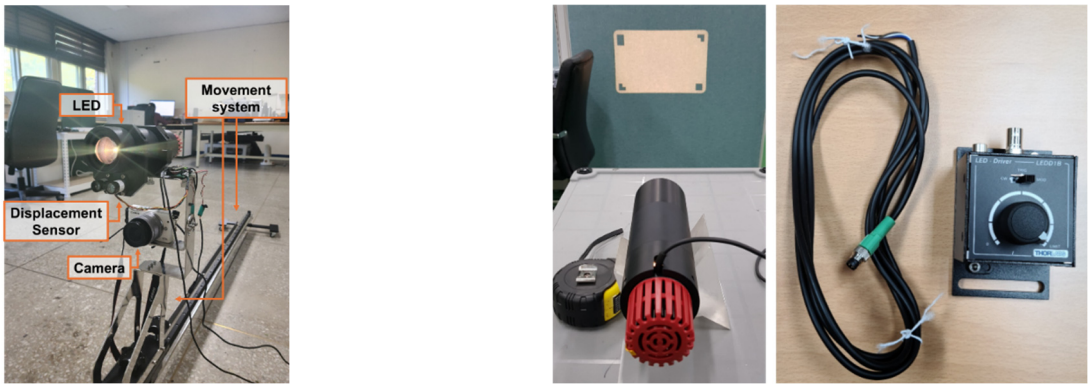

(a) Image acquisition system (b) Projected pattern of LED (left) and LED Driver (right)

Fig. 3 Image acquisition system and the projected pattern

Table 1 Image acquisition system main components

Component	Model	Specification
Camera	Canon EOS M10	Resolution: 5184 × 3456 pixel Dimension: 108 × 67 × 35 mm Image Sensor Type: CMOS Focal Length Multiplier: 1.6 Weight: 301 g
LED	Thorlabs MWWHLP1	Color: Warm White Correlated Color Temperature: 3000K Viewing Angle: 125° Weight: 650 g

(a) Entire image acquisition system with the movement system (b) Target(Steel Plate) and the movement system

Fig. 4 Movement system of the image acquisition system

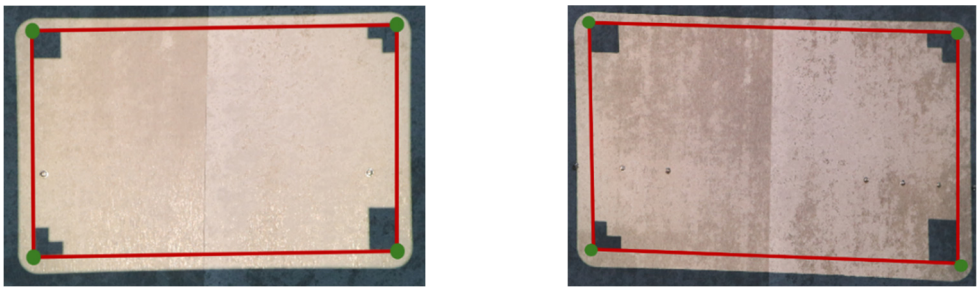

Fig. 5 Examples of detected corners (Green Circle) of the projected pattern

corner of the projected pattern, this step can be automated in future work using advanced computer vision algorithms mentioned in Related works section. The identified corner coordinates are then passed to the calibration stage, where they serve as key reference points for correcting geometric distortion and enabling accurate target measurement.

3.3 Target verficiation

After image pre-processing is applied to the images, image calibration algorithm is performed to make images face toward the main target. Note that calibration algorithm in this study denotes the conversion process to frontal view image. The calibration step requires two input images; a reference image, capture with the camera oriented perpendicular to the main target, and an input image taken from an arbitrary angle. In this paper, reference image is **A** and input image is denoted as **B**.

First, the four corner points, which are depicted in green circle in Fig. 5, of both **A** and **B** are identified and used as corresponding feature points where $\mathbf{a}_i = [u_i, v_i, 1]$ and $\mathbf{b}_i = [u_i', v_i', 1]$ are pixel coordinates of camera frames in **A** and **B** where $i = 1,2,3,4$. Using these point correspondences, a perspective matrix $\mathbf{P} \in \mathbb{R}^{3\times3}$ is estimated using getPerspectiveTransform() function in the OpenCV library based on the least square method. The perspective transformation equation is defined in Eq. (1).

$$\mathbf{x}' = \mathbf{P}\mathbf{x} \tag{1}$$

Where $\mathbf{x} = [u, v, 1]^T, \mathbf{x}' = [u', v', 1]^T$ are the homogeneous coordinates of points in **B** and **A**, and **P** is the perspective matrix mapping points from **B** to **A**. The computed **P** is then applied to image **B**, transforming it such that it appears as if captured from the same frontal perspective as **A** as shown in Fig. 6. This calibration procedure is repeated for all acquired images **B**. Each transformation required less than a second, indicating that the calibration is computationally efficient. Following calibration, the corrected images are used for analysis, in which the user manually measures target such as bolt widths or crack widths.

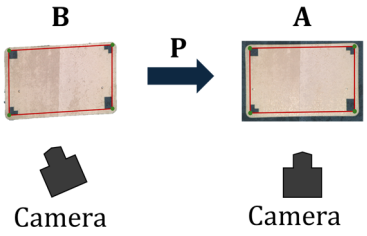

Fig. 6 Illustration of calibration based on the projected pattern

After the calibration process, all transformed images (**B**) are aligned to the reference perspective **A**, enabling consistent scale and geometry across the dataset. The user can then manually measure the target features such as crack width or bolt diameter directly from these corrected images, ensuring that measurements are not affected by perspective distortion.

4. Experimental results

4.1 Experimental setup

To evaluate the effectiveness of the proposed image acquisition system and the proposed framework, indoor and outdoor experiments were conducted. In the indoor experiment, a steel plate with eight bolts served as the primary target, while in the outdoor experiment, the camera was positioned inside a tunnel to capture images of cracks. To measure the accuracy, widths of the targets are manually calculated for both experiments. In this section, original image refers to the raw image taken by the proposed image acquisition system, and similarly calibrated image denotes the processed images which the proposed framework from section 3 is applied.

In both experiments, the root mean square error (RMSE) was employed as the evaluation metric, defined as

$$\text{RMSE} = \sqrt{\sum_{i=1}^{n} \frac{(\mathbf{B}_i^w - \mathbf{A}_i^w)^2}{n}} \tag{2}$$

(a) Image acquisition system

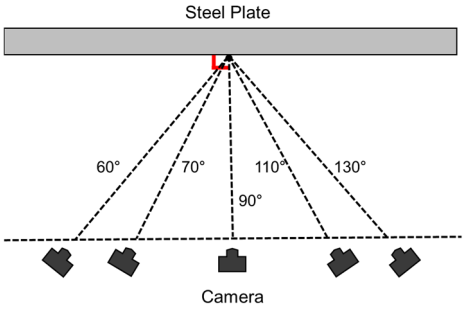

(b) Layout of the indoor experiment from the top view

Fig. 7 The image acquisition system for indoor experiment where (a) shows the entire setup; and (b) describes the layout from the top view

Where $\mathbf{A}_i^w$ represents the pixel width of the targets in the reference image, and $\mathbf{B}_i^w$ similarly denotes the pixel width of the targets in either the original or calibrated images.

4.2 Indoor experiment

In indoor experiment, a steel plate with eight bolts was attached to the movement system, and placed adjacent to a wall, which the bolts are main targets. Then, the camera system was first aligned to maintain a perpendicular (90°) angle to the plate from a top view, ensuring proper orientation using the movement system. Images were acquired by rotating camera to angles of 60°, 70°, 90°, 110° and 130°, where 90° corresponds to the perpendicular reference position to cover wide range of perspectives. For each angle, the distance between the camera system and the steel plate was adjusted to 160 cm, 180 cm, 200 cm, 220 cm, 240 cm, 260 cm, 280 cm and 300 cm. As a result, eight images were obtained for each angle, resulting in a total of 40 images. Fig. 7 shows the indoor experimental setup, including the steel plate mounted on the movement system.

After images are obtained, image pre-processing was performed to all images except for the perpendicular (90°) cases, resulting in 32 calibrated images. Total 72 images (original and calibrated) were obtained and used for performance evaluation, and pixel widths of eight bolts were carefully manually measured for all the images.

To be more specific, for each distance, the original

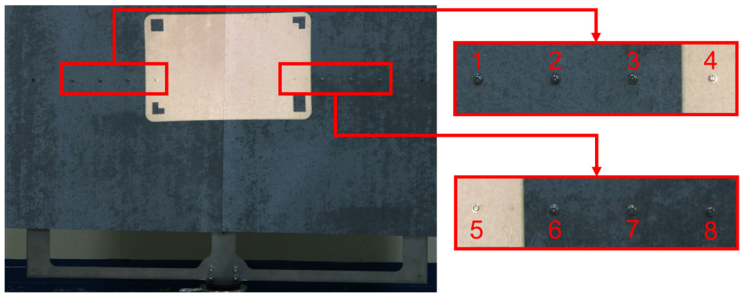

Fig. 8 The steel plate with bolts. Red boxes represent magnified visualization results of the bolts

Table 2 Comparison results of width average of eight bolts between original image and calibrated image for each angle (Bold values indicate best performance)

Angle	Original		Calibrated	
	RMSE(pixel)	Standard deviation (pixel)	RMSE(pixel)	Standard deviation (pixel)
		60°		
300 cm	1.822233382	2.563554	1.2263512	1.548121
280 cm	2.781873806	7.433103	2.3009067	5.248284
260 cm	3.050623789	8.784182	2.1261589	5.018715
240 cm	4.101595787	15.85139	2.6157755	8.652728
220 cm	5.141703548	28.94606	2.8157152	11.79512
200 cm	5.822836111	25.44203	4.869224	26.82748
180 cm	6.708150965	33.63702	4.3211472	23.20222
160 cm	6.918386273	48.83356	6.2742089	49.32405
Average	4.543425458	21.43636	**3.318686**	**16.45209**
		70°		
300 cm	2.467952188	6.229214	1.9234464	4.117023
280 cm	2.119729375	3.415136	1.3982014	1.794573
260 cm	2.108637949	4.526507	1.5364623	3.348825
240 cm	1.790158652	3.599198	1.0877915	1.473479
220 cm	2.518865469	12.05181	1.811996	6.835173
200 cm	1.821044686	3.667518	2.3955326	13.18144
180 cm	3.771815412	7.214118	1.8119571	2.354823
160 cm	4.584861067	22.61705	3.1223469	13.09861
Average	2.6478831	7.915068	**1.885967**	**5.775493**

Table 2 Continued

Angle	Original		Calibrated	
	RMSE(pixel)	Standard deviation (pixel)	RMSE(pixel)	Standard deviation (pixel)
		110°		
300 cm	1.038956869	0.933485	0.7029545	0.571038
280 cm	0.820761917	0.491142	0.5673013	0.249172
260 cm	1.585322089	2.680868	0.5921141	0.373735
240 cm	1.235438333	2.693834	1.1806973	2.476148
220 cm	2.869235591	11.30821	2.490116	7.629633
200 cm	3.677613934	9.902054	3.19669	12.23559
180 cm	4.218085703	11.33769	3.4199058	10.49326
160 cm	5.229238544	22.38215	4.1017189	18.75119
Average	2.584331623	7.716178	**2.031437**	**6.597471**
		130°		
300 cm	2.96195552	3.366791	1.7136831	2.764439
280 cm	1.650897786	3.605008	0.8817392	1.560051
260 cm	2.109570158	3.463363	1.461303	3.16655
240 cm	2.048607515	3.25466	1.3214064	1.126576
220 cm	2.901885982	7.882293	2.3788167	11.6431
200 cm	3.950887543	9.60336	2.6518241	10.1423
180 cm	5.170100144	17.23185	3.6661308	13.87539
160 cm	5.970810906	33.67423	5.1779709	29.60129
Average	3.345589444	10.26019	**2.406609**	**9.234962**
Total Average	3.280307406	11.832	**2.4106748**	**9.515**

image and the calibrated image were compared using the frontal view image (90°) at the same distance as the reference. Fig. 8 shows the steel plate used in the indoor experiment, including magnified views of the eight bolts that served as the main targets.

Table 2 summarizes the comparison results of original images and calibrated images for each angle varying distances. As described above, the pixel widths of bolts were measured, the average width was computed, and RMSE was computed for each original and calibrated image using the frontal view image as the reference. In this experiment, Eq. (2) was used for RMSE computation, where $\mathbf{A}_i^w$ represents bolt width of the reference image, and $\mathbf{B}_i^w$ denotes the pixel width of bolts of the original or calibrated images where $n = 8$ is the total number of bolts. In addition, the standard deviations were computed from the eight bolts for each configuration to quantify the variability of the results. Note that the standard deviations were computed from the error values $\mathbf{B}_i^w - \mathbf{A}_i^w$.

As shown in Table 2, calibrated images outperformed original images in most cases. To be more specific, RMSE was reduced by 26.9% at 60°, 28.8% at 70°, 21.4% at 110°, and 28.1% at 130°, compared to the original images. Similarly, standard deviation was reduced by 23.2% at 60°, 27.03% at 70°, 14.49% at 110°, and 19.58% at 130°. Overall, the total average RMSE decreased from 3.280 to 2.41, and the total average standard deviation decreased from 11.832 to 9.515, which can be observed in Fig. 9 that

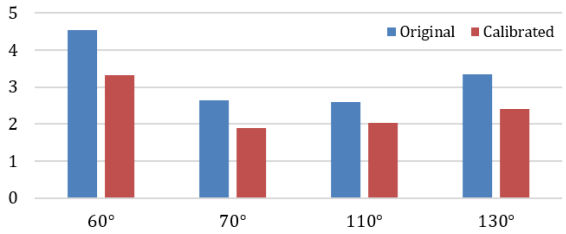

Fig. 9 Graph of average bolt width RMSE for original and calibrated images for each angle

represents the average RMSE graph of distances for each angle.

It is also observed that RMSE and standard deviation both tend to increase as the camera moves closer to the target. This is because, at shorter distances, the bolts appear larger in the image, which increases the effect of even small geometric distortions, causing higher measurement errors. Therefore, these results confirm that the proposed camera system improves the reliability of bolt width measurements under varying camera angles and distances, using the frontal view as a fixed reference.

Fig. 10 presents some visualization results of the images at 60° and 130° with identical distances where red boxes represent magnified results of bolts for better visualization. As observed in Fig. 10, the proposed system successfully calibrates the images in indoor environment when compared

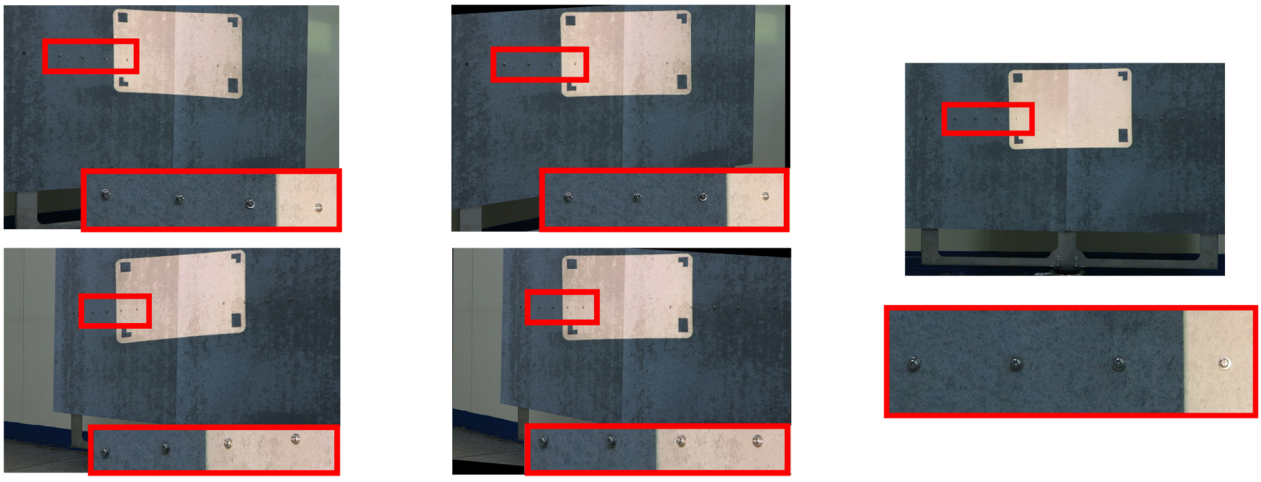

(a) Original (b) Calibrated (c) Ground Truth (frontal view)

Fig. 10 Visualization results acquired by the proposed system at 60°(top) and 130°(bottom) cases with 160 cm where red boxes represent magnified section of bolts

(a) (b)

Fig. 11 Image acquisition system for outdoor experiment

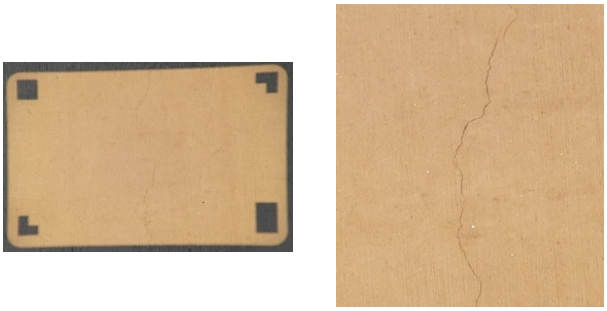

(a) (b)

Fig. 12 Part of crack (a) in tunnel where (b) represents the magnified section of the crack for better visualization

to frontal view reference. In Fig. 10(a) original image, both the bolts and the projected pattern are distorted due to camera angles. On the contrary, the calibrated images in Fig. 10(b) show improved results since the projected pattern and bolts match those in the frontal view reference image in Fig. 10(c). Although a slight residual distortion is still noticeable in the 130° calibrated image, the overall calibration accuracy demonstrates the robustness of the proposed system in mitigating angular distortion effects.

4.3 Outdoor experiment

For the outdoor experiment, images were captured in Gunsan, Republic of Korea. As illustrated in Fig. 11, the image acquisition system was mounted on the tripod and positioned inside an actual tunnel, and oriented toward a primary crack. Due to environmental constraints, the movement system was not employed in this experiment. The main target was the largest crack in the tunnel, which extended from the bottom to the top of the tunnel. Images were obtained by varying both the distance and the camera angle. To be more specific, two distances were considered: near and far. For each distance, three positions were selected: left, center (frontal view), and right, by manually shifting the camera system, and a total of six images were acquired. Fig. 12 presents the captured crack regions by the proposed system.

For performance evaluation, similar procedure as the indoor experiment was applied. All images are calibrated using the proposed approach except for the center images used as the main reference. Then, max width of crack was manually measured for each image, and compared to the corresponding center (reference) image at each distance. In this experiment, $\mathbf{A}_i^w$ represents max width of the crack (in pixels) in the reference image, and $\mathbf{B}_i^w$ denotes the max width of crack (in pixels) of the original or calibrated images where $n = 2$ represents left and right images for each distance setting.

Table 3 shows the maximum crack width measurements for each case, and Table 4 summarizes the average RMSEs between original/calibrated images and the reference image. In the near-distance case, the original images achieved an RMSE of 2.461 pixels, which was reduced to 2.022 pixels after applying the proposed framework, an improvement of approximately 17.8%. In the far-distance case, the proposed was also effective since RMSE dropped from 1.331 pixels

Table 3 Maximum crack widths in pixel for original and calibrated images in near and far cases

	Center	Original		Calibrated	
		Right	Left	Right	Left
		Near			
Max width (pixel)	7.992	4.926	6.345	5.591	6.438
		Far			
Max width (pixel)	6.626	4.913	5.847	6.491	6.076

Table 4 RMSE comparison of crack widths for original and calibrated images. Bold numbers indicate better performance

	Original RMSE (pixel)	Calibrated RMSE (pixel)
Near	2.461	**2.022**
Far	1.331	**0.400**
Average	1.896	**1.211**

to 0.400 pixels, corresponding to about 69.9% reduction in error. On average, the calibrated images achieved an RMSE of 1.211 pixels, compared to 1.896 pixels for the original images. This represents a 36.1% overall improvement in accuracy. These results demonstrate that the proposed image acquisition system is effective not only in controlled indoor environments but also in challenging outdoor environments.

In summary, the experimental results from both indoor and outdoor environments demonstrate the effectiveness of the proposed camera system. In the indoor experiment, which involved bolt width measurements under controlled conditions, the average RMSE across all angles decreased from 3.280 pixels in the original images to 2.411 pixels after calibration, resulting in about 26.5% improvement. The most notable reductions were observed at 70° and 130°, indicating the robustness of the system under varying oblique viewpoints and distances. In the outdoor experiment, conducted in tunnel environment, the proposed system also improved performance. The average RMSE dropped from 1.896 pixels to 1.211 pixels, yielding a 36.1% improvement in maximum crack width estimation. In the far-distance case, where perspective distortion is more severe, the RMSE was reduced by about 70%, further highlighting the system's capability. These findings confirm that the proposed image acquisition system significantly enhances geometric measurement accuracy in both idealized and actual environments, suggesting its practical applicability in structural inspection, tunnel monitoring, and related domains.

5. Conclusions

This study proposed a marker-free image acquisition system for accurate inspection measurement, eliminating the need for physical markers. The proposed system integrates a flexible image acquisition platform, an LED projection module with adjustable illuminance, a displacement sensor, and a flexible movement system which allows linear motion and rotations. These components enable geometric calibration and improved measurement reliability. Experimental validation in both indoor and outdoor environments demonstrated that the proposed methodology effectively minimizes geometric distortion, even under oblique camera angles, and achieves practical usability in field inspections with simple image processing algorithms.

However, this study has several limitations. First, the current implementation still requires manual selection of the projected pattern corners during the calibration process, which may reduce operational efficiency in large-scale inspections. Second, the outdoor experiments were conducted under limited distance and angle configurations, and the system's performance has not been comprehensively evaluated across a wide range of structural defect types or environmental conditions due to environmental constraints.

Future work will focus on additional experiments by conducting extended experiments across a broader range of structure, defect geometries, and environmental scenarios, particularly in outdoor field conditions. The integration of the proposed hardware with UAV platforms will also be explored, extending its applicability to large-scale infrastructure inspections. Furthermore, automating the corner detection process will be investigated in future work. Various computer vision methods can be applied such as traditional feature detection methods (SIFT, ORB, Harris corner), contour estimation techniques, and deep learning-based approaches. We plan to test various algorithms and optimize the corner detection process for full automation and robust corner detection under diverse environmental conditions.

Acknowledgments

This work was supported by 2025 Hannam University Research Fund. This work was also supported by the National Research Foundation of Korea (NRF) grant funded by the Korea government (Ministry of Science and ICT) (No. RS-2024-00415881).

References

Ali, A., Sandhu, T.Y. and Usman, M. (2019), "Ambient vibration testing of a pedestrian bridge using low-cost accelerometers for SHM applications", *Smart Cities*, **2**(1), 20-30. https://doi.org/10.3390/smartcities2010002

Bhowmick, S., Nagarajaiah, S. and Veeraraghavan, A. (2020), "Vision and deep learning-based algorithms to detect and quantify cracks on concrete surfaces from UAV videos", *Sensors*, **20**(21), p. 6299. https://doi.org/10.3390/s20216299

Canny, J. (1986), "A computational approach to edge detection", *IEEE Transact. Pattern Anal. Mach. Intell.*, (6), 679-698. https://doi.org/10.1109/TPAMI.1986.4767851

Ding, W., Yang, H., Yu, K. and Shu, J. (2023), "Crack detection and quantification for concrete structures using UAV and transformer", *Automat. Constr.*, **152**, p. 104929.

https://doi.org/10.1016/j.autcon.2023.104929
Dorafshan, S., Thomas, R.J. and Maguire, M. (2018), "Comparison of deep convolutional neural networks and edge detectors for image-based crack detection in concrete", *Constr. Build. Mater.*, **186**, 1031-1045. https://doi.org/10.1016/j.conbuildmat.2018.08.011
Dosovitskiy, A., Beyer, L., Kolesnikov, A., Weissenborn, D., Zhai, X., Unterthiner, T., Dehghani, M., Minderer, M., Heigold, G., Gelly, S., Uszkoreit, J. and Houlsby, N. (2020), "An image is worth 16x16 words: Transformers for image recognition at scale", arXiv preprint arXiv:2010.11929.
Feng, S., Gao, M., Jin, X., Zhao, T. and Yang, F. (2024), "Fine-grained damage detection of cement concrete pavement based on UAV remote sensing image segmentation and stitching", *Measurement*, **226**, p. 113844. https://doi.org/10.1016/j.measurement.2023.113844
Fernandez-Navamuel, A., Pardo, D., Magalhães, F., Zamora-Sánchez, D., Omella, Á.J. and Garcia-Sanchez, D. (2025), "Deep neural network for damage detection in Infante Dom Henrique bridge using multi-sensor data", *Struct. Health Monitor.*, **24**(1), 372-401. https://doi.org/10.1177/14759217241227455
Kang, M. and An, S.Y.K. (2024), "Crack growth prediction on a concrete structure using deep ConvLSTM", *Smart Struct. Syst., Int. J.*, **33**(4), 301-311. https://doi.org/10.12989/sss.2024.33.4.301
Kaveh, H. and Alhajj, R. (2024), "Recent advances in crack detection technologies for structures: A survey of 2022-2023 literature", *Front. Built Environ.*, **10**, p. 1321634. https://doi.org/10.3389/fbuil.2024.1321634
Kim, H., Ahn, E., Cho, S., Shin, M. and Sim, S.H. (2017a), "Comparative analysis of image binarization methods for crack identification in concrete structures", *Cement Concrete Res.*, **99**, 53-61. https://doi.org/10.1016/j.cemconres.2017.04.018
Kim, H., Lee, J., Ahn, E., Cho, S., Shin, M. and Sim, S.H. (2017b), "Concrete crack identification using a UAV incorporating hybrid image processing", *Sensors*, **17**(9), p. 2052. https://doi.org/10.3390/s17092052
Krizhevsky, A., Sutskever, I. and Hinton, G.E. (2012), "Imagenet classification with deep convolutional neural networks", *Adv. Neural Inform. Process. Syst.*, **25**. https://doi.org/10.1177/1475921719898862
Kumar, P., Batchu, S. and Kota, S.R. (2021), "Real-time concrete damage detection using deep learning for high rise structures", *IEEE Access*, **9**, 112312-112331. https://doi.org/10.1109/ACCESS.2021.3102647
Lee, J.H., Yoon, S., Kim, B., Gwon, G.H., Kim, I.H. and Jung, H.J. (2021), "A new image-quality evaluating and enhancing methodology for bridge inspection using an unmanned aerial vehicle", *Smart Struct. Syst., Int. J.*, **27**(2), 209-226. https://doi.org/10.12989/sss.2021.27.2.209
Lei, B., Ren, Y., Wang, N., Huo, L. and Song, G. (2020), "Design of a new low-cost unmanned aerial vehicle and vision-based concrete crack inspection method", *Struct. Health Monitor.*, **19**(6), 1871-1883. https://doi.org/10.1177/1475921719898862
Li, H.Y., Huang, C.Y. and Wang, C.Y. (2023), "Measurement of cracks in concrete bridges by using unmanned aerial vehicles and image registration", *Drones*, **7**(6), p. 342. https://doi.org/10.3390/drones7060342
Meng, S., Gu, L., Zhou, Y. and Jafari, A. (2024), "A label-free high precision automated crack detection method based on unsupervised generative attentional networks and swin-crackformer", *Smart Struct. Syst., Int. J.*, **33**(6), 449-463. https://doi.org/10.12989/sss.2024.33.6.449
Moore, M., Phares, B.M., Graybeal, B., Rolander, D., Washer, G. and Wiss, J. (2001), "Reliability of visual inspection for highway bridges", Volume I (No. FHWA-RD-01-105), Turner-Fairbank Highway Research Center.
Munawar, H.S., Hammad, A.W., Waller, S.T. and Islam, M.R. (2022), "Modern crack detection for bridge infrastructure maintenance using machine learning", *Human-Centric Intell. Syst.*, **2**(3), 95-112. https://doi.org/10.1007/s44230-022-00009-9
Ni, Y., Mao, J., Wang, H., Xi, Z. and Xu, Y. (2023), "Toward high-precision crack detection in concrete bridges using deep learning", *J. Perform. Constr. Facil.*, **37**(3), p. 04023017. https://doi.org/10.1061/JPCFEV.CFENG-4275
Peng, X., Duan, B., Zhou, K., Zhong, X., Li, Q. and Zhao, C. (2024), "UAV-based bridge crack discovery via deep learning and tensor voting", *Smart Struct. Syst., Int. J.*, **33**(2), 105-118. https://doi.org/10.12989/sss.2024.33.2.105
Rehman, S.U., Usman, M., Toor, M.H.Y. and Hussaini, Q.A. (2024), "Advancing structural health monitoring: A vibration-based IoT approach for remote real-time systems", *Sensors Actuat. A: Phys.*, **365**, p. 114863. https://doi.org/10.1016/j.sna.2023.114863
Tanveer, M. and Cho, S. (2025), "Unsupervised deep learning method for concrete and asphalt crack segmentation using vision transformer and probability thresholding", *Smart Struct. Syst., Int. J.*, **35**(5), 267-284. https://doi.org/10.12989/sss.2025.35.5.267
Tian, F., Zhao, Y., Che, X., Zhao, Y. and Xin, D. (2019), "Concrete crack identification and image mosaic based on image processing", *Appl. Sci.*, **9**(22), p. 4826. https://doi.org/10.3390/app9224826
Wang, G., Wang, K.C., Zhang, A.A. and Yang, G. (2023), "A deep and multiscale network for pavement crack detection based on function-specific modules", *Smart Struct. Syst., Int. J.*, **32**(3), 135-151. https://doi.org/10.12989/sss.2024.33.6.449
Wang, J., Wang, P., Qu, L., Pei, Z. and Ueda, T. (2024), "Automatic detection of building surface cracks using UAV and deep learning-combined approach", *Struct. Concrete*, **25**(4), 2302-2322. https://doi.org/10.1002/suco.202300937
Xu, Y. and Turkan, Y. (2020), "BrIM and UAS for bridge inspections and management", *Eng. Constr. Archit. Manag.*, **27**(3), 785-807. https://doi.org/10.1108/ECAM-12-2018-0556
Yoon, S., Lee, Y.-J. and Jung, H.-J. (2018), "A comprehensive framework for seismic risk assessment of urban water transmission networks", *Int. J. Disaster Risk Reduct.*, **31**, 983-994. https://doi.org/10.1016/j.ijdrr.2018.09.002
Yoon, S., Lee, Y.-J. and Jung, H.-J. (2020a), "A comprehensive approach to flow-based seismic risk analysis of water transmission network", *Struct. Eng. Mech., Int. J.*, **73**(3), 339-351. https://doi.org/10.12989/sem.2020.73.3.339
Yoon, S., Lee, Y.-J. and Jung, H.-J. (2020b), "Accelerated Monte Carlo analysis of flow-based system reliability through artificial neural network-based surrogate models", *Smart Struct. Syst., Int. J.*, **26**(2), 175-184. https://doi.org/10.12989/sss.2020.26.2.175
Yoon, S., Lee, Y.-J. and Jung, H.-J. (2021a), "Flow-based seismic resilience assessment of urban water transmission network", *Struct. Eng. Mech., Int. J.*, **79**(4), 517-529. https://doi.org/10.12989/SEM.2021.79.4.517
Yoon, S., Gwon, G.-H., Lee, J.-H. and Jung, H.-J. (2021b), "Three-dimensional image coordinate-based missing region of interest area detection and damage localization for bridge visual inspection using unmanned aerial vehicles", *Struct. Health Monitor.*, **20**(4), 1462-1475. https://doi.org/10.1177/1475921720918675
Yoon, S., Lee, S., Kye, S., Kim, I.H., Jung, H.J. and Spencer Jr, B.F. (2022a), "Seismic fragility analysis of deteriorated bridge structures employing a UAV inspection-based updated digital twin", *Struct. Multidiscipl. Optimiz.*, **65**(12), p. 346. https://doi.org/10.1007/s00158-022-03445-0
Yoon, S., Spencer Jr, B.F., Lee, S., Jung, H.J. and Kim, I.H.

(2022b), "A novel approach to assess the seismic performance of deteriorated bridge structures by employing UAV-based damage detection", *Struct. Control Health Monitor.*, **29**(7), p. e2964. https://doi.org/10.1002/stc.2964

Yuan, Q., Shi, Y. and Li, M. (2024), "A review of computer vision-based crack detection methods in civil infrastructure: Progress and challenges", *Remote Sensing*, **16**(16), p. 2910. https://doi.org/10.3390/rs16162910

Zhang, Y., Liu, P. and Zhao, X. (2021), "Structural displacement monitoring based on mask regions with convolutional neural network", *Constr. Build. Mater.*, **267**, p. 120923. https://doi.org/10.1016/j.conbuildmat.2020.120923

Zhong, X., Peng, X., Yan, S., Shen, M. and Zhai, Y. (2018), "Assessment of the feasibility of detecting concrete cracks in images acquired by unmanned aerial vehicles", *Automat. Constr.*, **89**, 49-57. https://doi.org/10.1016/j.autcon.2018.01.005

Zhu, Q., Dinh, T.H., Hoang, V.T., Phung, M.D. and Ha, Q.P. (2018), "Crack detection using enhanced thresholding on UAV based collected images", arXiv preprint arXiv:1812.07868.